Measurement 269 (2026) 120757

Contents lists available at ScienceDirect

Measurement

journal homepage: www.elsevier.com/locate/measurement

# On the electrochemical behavior of a novel bixbyite-structured high-entropy oxide as a possible solid electrolyte

Filippo Milano [a,b,*], Antonio Vendittelli [a,b], Luca Spiridigliozzi [c,d,e], Viviana Monfreda [e,f], Gianfranco Dell'Agli [d,e,f], Luigi Ferrigno [a,b]

[a] University of Cassino and Southern Lazio, Department of Electrical and Information Engineering, Cassino, 03043, Italy
[b] European University of Technology, European Union, Cassino, 03043, Italy
[c] Universitas Mercatorum, Department of Engineering and Science, Roma, 00186, Italy
[d] National Interuniversity Consortium of Materials Science and Technology (INSTM), Firenze, 50121, Italy
[e] EUT+ Institute of Nanomaterials and Nanotechnologies-EUTINN, European University of Technology, European Union, Cassino, 03043, Italy
[f] University of Cassino and Southern Lazio, Department of Civil and Mechanical Engineering, Cassino, 03043, Italy

ARTICLE INFO

*Keywords:*
High-entropy oxides
Electrochemical impedance spectroscopy
Experimental characterization
Solid electrolytes

ABSTRACT

The present study investigates the thermal behavior and electrochemical response of a novel bixbyite-structured high-entropy oxide, $(Ce_{0.2}Zr_{0.2}Yb_{0.2}Er_{0.2}Nd_{0.2})_2O_{3+\delta}$ (CZYEN), fabricated as a possible candidate for solid electrolyte applications. Due to their ultralow thermal conductivity and entropy-driven stability, rare-earth-based high-entropy oxides, i.e. the class of materials to which CZYEN belongs offer an interesting platform to explore the thermal transient phenomena often overlooked in impedance-based characterizations. Thus, using Electrochemical Impedance Spectroscopy (EIS) across a temperature range of 500 – 800 °C and a detailed time-resolved protocol, this study aims to quantify the discrepancy between furnace set-point and true specimen temperature, revealing significant transitory dynamics prior to thermal equilibrium. The evolution of the Nyquist plot area and equivalent circuit parameters, especially the charge transfer resistance $(R_p)$, exhibited exponential trends with time, reflecting the gradual heat diffusion through the system. Our results highlight the critical need for extended thermal equilibrium periods in EIS measurements of low thermal conductivity ceramic materials. In fact, for all the investigated temperatures, a thermal transient lasting several hours and a thermal dynamics variable with the oven temperature were found To this regards, the proposed methodology enhances the reliability of electrochemical characterizations and underlines the importance of accounting for thermal transients in low-conductive solid oxides.

## 1. Introduction

The pursuit of safer and higher-power electrochemical energy devices has shifted attention towards solid ceramic electrolytes, i.e. dense oxide materials whose purely ionic or mixed ionic–electronic conductivities are the core principle of solid-oxide fuel cells, oxygen-separation membranes, solid-state lithium batteries and a growing class of catalytic membrane reactors [1–3]. Their performance, longevity and failure modes are ultimately governed by ion transport phenomena occurring on length-scales that span the bulk lattice, micrometers-thin grain boundaries and the often nanometers-thin electrochemical interface to metallic current collectors or gaseous reactants. A clear understanding of these complex electrochemical features is therefore essential to reliably deconvolute the different contributions in the impedance spectrum and to extract physically meaningful parameters useful for materials design.

Electrochemical Impedance Spectroscopy (EIS) [4,5] can be considered as the most versatile and non-destructive technique for probing multiscale transport in solids [3]. Through the application of a small-amplitude sinusoidal perturbation over several decades of frequency, the EIS records the complex impedance useful for distinguishing the different relaxation processes occurring within a material. EIS-based approaches have also been used in literature for the characterization of biological tissues, such as human skin, where the measured frequency-dependent electrical response reflects the functional state of the system under investigation [6]. Furthermore, by performing EIS measurements at successive time instants, it is possible to obtain a time-varying

* Corresponding author at: University of Cassino and Southern Lazio, Department of Electrical and Information Engineering, Cassino, 03043, Italy.
*E-mail addresses:* filippo.milano@unicas.it (F. Milano), antonio.vendittelli@unicas.it (A. Vendittelli), luca.spiridigliozzi@unimercatorum.it (L. Spiridigliozzi), viviana.monfreda@unicas.it (V. Monfreda), dellagli@unicas.it (G. Dell'Agli), ferrigno@unicas.it (L. Ferrigno).

https://doi.org/10.1016/j.measurement.2026.120757
Received 23 October 2025; Received in revised form 15 January 2026; Accepted 6 February 2026
Available online 11 February 2026

impedance response that provides information on the temporal evolution of electrical quantities correlated with the functional state of the system under test. For example, repeated EIS measurements have been used in literature to monitor the evolution of cement-based materials over extended periods, yielding insights into hydration-related processes [7].

In dense oxide electrolytes, the high-frequency intercept of the Nyquist plot primarily reflects the bulk (lattice) resistance of the electrolyte (because interfacial polarization and diffusion-related processes are negligible at such high frequency), the intermediate-frequency arc refers to grain-boundary blocking effects, and either a low-frequency semicircle or a Warburg-type straight line captures the coupled charge-transfer and chemical capacitance of the electrode/electrolyte interface [3]. Equivalent electric models have allowed researchers to extract not only bulk ionic conductivity and electronic transference numbers but also grain-boundary capacitance, defect formation enthalpies and surface-exchange coefficients [8–12].

Yet the reliability of any parameter deduced from such fitting depends critically on the experimental set-up of the EIS analysis.

Even modest alterations in specimen fabrication, electrode design or instrumental configuration can shift or distort the impedance response in a way that hides the true behavior of the materials. For example, porosity, micro-cracks or nano-grained morphologies introduce additional constriction and space-charge resistances that masquerade as bulk or grain-boundary arcs, thereby skewing apparent activation energies. Inappropriate choice suppresses or amplifies the low-frequency feature, producing erroneous estimates of interfacial kinetics or transference numbers. Consequently, the quality of an EIS data set is inseparable from the quality of the experimental conditions used for collecting it. Consensus best practice from literature [13–15] includes: (i) highly dense (≥95% of theoretical) pellets; (ii) symmetric two-electrode cells with well-defined, reproducible contact areas; (iii) four-terminal lead configurations coupled to short wiring to suppress parasitic phenomena; (iv) periodic instrument calibration across the entire frequency span of interest. However, an additional yet fundamental aspect to account for (especially for solid ceramic electrolytes), is the accurate knowledge of true specimen temperature upon EIS measurements. Because both the resistive and capacitive elements of ceramic electrolytes obey Arrhenius-type relations [3], a systematic error of merely 5–10 °C at 800 °C translates into ≥10 % uncertainty in the bulk conductivity and into comparable deviations in the grain-boundary and electrode estimated activation energies. Such errors (derived to the lack of knowledge about true specimen temperature) commonly arise when the set-point of the furnace controller is accepted as the specimen temperature: radiative losses, convective gas cooling, imperfect thermal contact with alumina holders and axial gradients in common laboratory furnaces routinely depress the actual pellet temperature according to its thermal properties (i.e. thermal diffusivity and thermal conductivity, being almost always very low for ceramic electrolytes). To prevent this bias, one should ideally employ a fine-gauge thermocouple spring-loaded directly onto the electrolyte under test (while a second probe should monitor the furnace free-space), and only when the two readings converge one should initiate the impedance sweeps. However, to the best of our knowledge, it is hard to find such an experimental set-up configuration in literature concerning ceramic electrolytes EIS characterization, considering its practical complexity too.

Based on this analysis, this paper aims to investigate (by selecting a bixbyite-structured rare-earth-based high-entropy oxide) the dependence of EIS measurements of ceramic solid electrolytes on the time evolution of the temperature inside these materials. "High-entropy material" is a term commonly referred to a novel class of materials [16] exhibiting high-configurational entropies (i.e. $S_{config} > 1.5\,R$) [17], even if the reversibility of the entropy-driven stabilization at high-temperature is not explicitly demonstrated (as in that case, the term "entropy-stabilized materials" is used [18]). Particularly, bixbyite-structured rare-earth-based high-entropy oxides belong to a subclass of high-entropy materials recently known to be one exhibiting the lowest thermal conductivities at all [19]. In other words, our investigation was aimed at defining a measurement procedure tested on a bixbyite-structured high-entropy oxide, whose chemical composition is $\left(Ce_{0.2}Zr_{0.2}Yb_{0.2}Er_{0.2}Nd_{0.2}\right)_2 O_{3+\delta}$, to demonstrate the relevance of the thermal transient in such systems and, by analyzing its EIS-related features, to provide valuable guidelines to researchers in the field to correctly characterize their electrochemical behavior through reliable EIS measurements.

This paper is organized as follows. Section 2 provides an in-depth look at the electrolyte realization and assembly of the tested system, while Section 3 describes in detail the experimental set-up and the characterization procedure carried out, Section 4 discusses the obtained results, and finally the Conclusions are provided.

## 2. A brief note of the proposed material

The choice of a single-phase, bixbyite-structured (i.e. a defective fluorite-like structure high-entropy oxide [20]) whose chemical composition is $\left(Ce_{0.2}Zr_{0.2}Yb_{0.2}Er_{0.2}Nd_{0.2}\right)_2 O_{3+\delta}$ - labeled as CZYEN in the following - as the test electrolyte for our work provides a rigorous platform for highlighting temperature-related biases in EIS measurements. The "$O_{3+\delta}$" notation was adopted because, for bixbyite sesquioxides containing a significant fraction of tetravalent cations, oxygen-excess nonstoichiometry is the energetically preferred charge-compensation route predicted by atomistic defect calculations, and it has also been observed crystallographically in oxidized bixbyite solid solutions [20–22]. From a defect-chemistry perspective, bixbyite (C-type sesquioxide) differs from the typical fluorite-like vacancy conductors (e.g., YSZ, doped ceria), as its lowest-energy intrinsic disorder mechanism is predicted to be oxygen Frenkel formation, i.e. the coupled formation of an oxygen vacancy and an oxygen interstitial, rather than a predominantly vacancy-rich Schottky defects network. This feature is attributed to the existence of a relatively large interstitial site in the bixbyite lattice capable of accommodating oxygen [21]. Therefore, oxygen interstitial defects are part of the natural defect landscape of bixbyite, and oxygen transport mechanisms based on interstitial motion are plausible in this structure type. More importantly, for our specific chemistry, atomistic modeling of aliovalent dopants in bixbyite sesquioxides indicates that tetravalent substitution on trivalent cation sites is preferentially charge-compensated by oxygen interstitial formation (rather than by cation vacancies or other mechanisms), with the oxygen interstitial occupying the 16c site [20,21]. This directly implies oxygen uptake ($\delta > 0$) under oxidizing conditions when a substantial fraction of the cation sublattice is tetravalent, as in the CZYEN composition. Definitely, even if the ionic conduction via interstitial oxygen is a less common phenomenon, it has already been reported both in bixbyite-like systems and other complex systems [23]. Anyway, because of its high configurational entropy and the very low thermal conductivities of rare-earth-based high-entropy oxides [19,24,25], this testing material is deemed perfect to highlight any mismatch between the nominal furnace temperature and the true specimen temperature. In other words, we believe that a bixbyite-structured high-entropy oxide is an ideal sample for isolating and quantifying the influence of real sample temperature on the collected impedance spectra.

### 2.1. Rationale of the material choice

The choice of CZYEN was based on prior development of rare-earth-based high-entropy oxides processed via carbonate co-precipitation, which has shown to be particularly effective in producing highly reactive precursors and, consequently, dense entropy-stabilized single phases under relatively mild sintering treatments. In our earlier work [26] we systematically investigated closely related rare-earth-based high-entropy oxides compositions containing the same core

cation set, demonstrating near-full densification at 1300 °C for Zr-containing systems and reporting intermediate-temperature conductivities of the same order of magnitude expected for ceria-based oxide conductors in air. Furthermore, to the best of our knowledge, the exact CZYEN bixbyite composition investigated here has not been previously reported as a dense bulk electrolyte with time-resolved EIS characterization. More broadly, the literature does include dense bixbyite-structured high-entropy sesquioxides or parent fluorite-structured high-entropy oxides [27], but pure bixbyites have been primarily developed for thermophysical or functional applications other than potential solid-electrolytes. For example, cubic bixbyite high-entropy $RE_2O_3$ ceramics have been designed and consolidated (e.g., by SPS) for thermal-barrier/CMAS (Calcium–Magnesium–Alumino–Silicate)-resistance studies [28]. In addition, a very closely related Ce–Zr containing high-entropy bixbyite has been synthesized by some of the authors as a stable and high-performing visible-light-active photocatalyst for multifunctional pollutant degradation [29].

### 2.2. Electrolyte fabrication

Cerium (III) nitrate ($Ce(NO_3)_3 \cdot 6H_2O$, Carlo Erba Reagents, Italy), ytterbium (III) nitrate ($Yb(NO_3)_3 \cdot 5H_2O$, Merck, Italy), neodymium (III) nitrate ($Nd(NO_3)_3 \cdot 5H_2O$, Merck, Italy), erbium (III) nitrate ($Er(NO_3)_3 \cdot 5H_2O$, Merck, Italy) and zirconium (IV) oxynitrate ($ZrO(NO_3)_2$, Carlo Erba Reagents, Italy) were used as metal precursors, while ammonium carbonate ($(NH_4)_2CO_3$, purity > 99,0%, Fluka-Honeywell, Germany) was used as precipitating agent for the synthesis of $(Ce_{0.2}Zr_{0.2}Yb_{0.2}Er_{0.2}Nd_{0.2})_2O_{3+\delta}$ (CZYEN). All chemical reagents were used as received from the supplier, without any further lab purification or thermal/chemical pre-treatment.

The synthesis procedure adopted for CZYEN can be summarized as follows: (i) all rare-earth nitrates were dissolved in deionized water to obtain a total cation concentration of 0.1 *M* (corresponding to 0.02 *M* for each individual cation); (ii) the cations-containing solution, hereafter referred to as Solution A, was vigorously stirred to ensure complete dissolution; (iii) a separate precipitating solution (labeled as Solution B) was prepared by dissolving an appropriate amount of ammonium carbonate in deionized water to achieve a carbonate-to-cation molar ratio (R) of 10; (iv) Solution B was then rapidly added to Solution A under mild stirring, leading to the immediate formation of a light-pinkish precipitate; (v) the resulting suspension was filtered under vacuum, thoroughly washed with deionized water, and dried overnight at 80 °C in static air.

The as-obtained CZYEN powder was subsequently calcined at 800 °C to favor the thermal decomposition of the as-synthesized precursors and to induce the formation of the desired bixbyite-like phase [30]. Ammonium carbonate was selected as the precipitating agent over possible alternatives such as ammonia or alkaline hydroxides, as it leads to well-reactive powders in ceria-based systems [31] so favoring the kinetics of obtaining the designed single phase [32]. The calcined CZYEN powder was uniaxially pressed into a cylindrical pellet with a diameter of 13 mm and subsequently sintered in static air at 1300 °C for 3 h (adopting a constant heating rate of 10 °C/min). The crystalline structure of both the as-prepared and the calcined samples were analyzed using X-ray diffraction with a Panalytical (Almelo, The Netherlands) XPERT MPD diffractometer (see Figure S1 and Figure S2 within the Supplementary Material). The as-prepared sample is an amorphous system presenting several broad peaks attributable to the bixbyite-like rare earth oxide (as always observed in previous works for co-precipitated rare-earth-based high-entropy oxides in carbonate environments), whilst the calcined sample exhibit all peaks attributable to a pure bixbyite-like reference structure (ICDD card n. 01-077-0458 referred to $Yb_2O_3$). The sintered pellet's density, determined by the Archimedes method using a highly sensitive analytical balance (Gibertini, Italy), together with its relative density calculated using the theoretical crystallographic density of CZYEN derived according to the indications shown in [33], are reported in Table 1. As can be seen from the obtained results, the material is fully dense.

**Table 1**
Theoretical and measured density of the tested sample.

| Property | Value |
|---|---|
| Chemical composition | $(Ce_{0.2}Zr_{0.2}Yb_{0.2}Er_{0.2}Nd_{0.2})_2O_{3+\delta}$ |
| Theoretical density [g/cm$^3$] | 7.32 |
| Measured density [g/cm$^3$] | 7.33 ± 0.02 |

Figure S3 within the Supplementary Material shows an exemplary micrograph taken at a rather low magnification of the sintered CZYEN electrolyte.

### 2.3. Cell assembly

To test the proposed solid electrolyte, a common symmetric cell scheme has been adopted [34] where Ag has been used as both electrodes. More specifically, a silver conductive paste has been painted on both sides of the sintered electrolyte and dried overnight at 70 °C.

The assembled $Ag|CZYEN|Ag$ cell was then subjected to a dedicated high-temperature conditioning step prior to any EIS acquisition: after painting and drying, the full cell was thermally treated at 800 °C for 1 h before starting the impedance measurements. Such pre-anneal promoted densification and stabilization of the Ag contact layer and of the Ag–electrolyte contact, so that subsequent EIS spectra are not collected during an evolving electrode state.

In such configuration, the fabricated cell working principle is briefly discussed hereafter, considering that in tetravalent-doped bixbyites the charge carrier is the incorporated interstitial oxygen [20,21] according to the following defect equation:

$$2ZrO_2 \xrightarrow{RE_2O_3} 2Zr^{\bullet}_{RE} + 3O^{x}_{O} + O''_{i}. \quad (1)$$

The half-cell reactions can be expressed as follows: on the negative electrode electrons are supplied externally as for the following reaction (lower $p_{O2}$):

$$\frac{1}{2} \cdot O_2(g) + 2e' \rightarrow O''_i, \quad (2)$$

while on the positive electrode, upon $O''_i$ moving through the CZYEN electrolyte, molecular oxygen is produced (higher $p_{O2}$) as for the following reaction:

$$O''_i \rightarrow \frac{1}{2} \cdot O_2(g) + 2e'. \quad (3)$$

Such electrode reactions occur at the interface between Ag and CZYEN, the fabricated cell being structured as follows: $Ag|CZYEN|Ag$ (considering eventual Ag oxidation phenomena as negligible). Thus, the half-cell reactions occurring at the electrode/electrolyte interfaces are responsible for the overall conduction of the solid electrolyte measured via EIS.

## 3. The experimental characterization

This Section presents the experimental approach used for the electrochemical characterization of the CZYEN electrolyte. An experimental campaign was conducted to evaluate the impedance of the electrolyte, via EIS, as temperature changes.

### 3.1. The experimental set-up

To carry out the experimental characterization, an experimental set-up was realized consisting of the following components.

- As described in the previous Section 2, a symmetric cell has been assembled by coating the two CZYEN electrolyte sides with a conductive silver paste (Nanografi, Turkey); subsequently, two copper wires were soldered onto the silver electrodes to ensure the physical connection to the impedance meter.
- A high-performance impedance meter for the application of EIS; specifically, the Gamry Reference 3000 was used. The instrument was used in a two-electrode potentiostatic configuration, applying a potential of 1 $V_{rms}$ in the frequency range from 100 Hz to 1 MHz.
- A furnace to perform the tests at variable and controlled temperatures; specifically, the Lenton furnaces was used. The temperature range explored goes from 500 °C up to 800 °C.
- a PC connected to the impedance meter, via USB interface, to manage the measurement process.

### 3.2. The measurement protocol

To carry out the experimental characterization of the electrolyte through the EIS at varying temperature, a specifically designed measurement protocol was followed, detailed below in all its phases.

(i) **Instrument tuning:** after a warm-up phase, the impedance meter is calibrated in order to eliminate systematic errors and compensate for the influence of any auxiliary components in the experimental set-up.
(ii) **Test temperature selection:** set the generic test temperature $T_i \in \{500, 600, 700, 800\}$ °C and wait for the furnace to reach the thermal regime. Therefore, in total we considered four different test temperatures.
(iii) **Test time instant selection:** for each selected temperature, several EIS measurements were performed as time varies; specifically, we consider the generic time instant $t_j \in \{0, 0.5, 1, \dots, 4.5\}$ $h$. Therefore, in total we considered ten different time instants.
(iv) **Impedance measurement:** for each selected temperature and time instant, three repeated EIS measurements are performed according to the amplitude and frequency settings detailed previously.
(v) **End:** the experimental characterization is finished.

Figs. 1 and 2 show the EIS measurements, obtained for all temperature and time instant conditions considered, by rectangular and polar impedance representation, respectively. All impedance measurements are also accompanied by the uncertainties of the various components (real part, imaginary part, modulus and phase) obtained by following the indications provided by the instrument datasheet [35].

It is very interesting to note that for all the investigated temperatures, the time instant at which the test is performed plays a very important role: in fact, when the furnace reaches the thermal regime we can assume that the metallic electrodes almost immediately reach the same temperature (due to very high Ag thermal conductivity [36]); conversely the CZYEN electrolyte, being part of a family of rare-earth-based high-entropy oxides known for exhibiting ultralow thermal conductivities [37] (i.e. almost three order of magnitudes less than Ag) and diffusivities certainly needs a certain amount of time (still depending on the considered temperature, as thermal diffusivity itself is dependent on temperature) to reach the thermal regime (corresponding to the furnace temperature).

## 4. Results and discussion

The goal of this Section is to characterize the thermal behavior of the tested cell, i.e. the Ag|$CZYEN$|Ag cell, in order to understand how the thermal transitory period affects the EIS measurements, especially considering the strong difference in terms of thermal properties between the metallic electrodes and the high-entropy ceramic electrolyte.

**Table 2**
Fitting output of the normalized result of the integral using the model shown in (6).

| T [°C] | $\tau$ [h] | RMSE |
|---|---|---|
| 500 | 0.727 | 0.013 |
| 600 | 0.661 | 0.012 |
| 700 | 0.634 | 0.011 |
| 800 | 0.607 | 0.007 |

A first common attribute found in all Nyquist plots as the temperature varies (see Fig. 1) is a narrowing of the diagram, both in width and height, as the time in which the EIS measurements were performed increases. Therefore, in order to evaluate the time needed for the electrolyte to reach thermal equilibrium, the area under the Nyquist plot was extracted as a feature according to the following integral

$$\int_{C_{ij}} -\Im\{\dot{Z}_{ij}\}\, d\Re\{\dot{Z}_{ij}\} = \alpha_{ij}, \quad \forall i = 1, 2, 3, 4 \text{ and } j = 1, 2, \dots, 10, \tag{4}$$

where $C_{ij}$ represents the path (the curve) traced by the Nyquist plot in the $(\Re\{\dot{Z}_{ij}\},\ -\Im\{\dot{Z}_{ij}\})$ plane obtained for the generic temperature $T_i$ and time instant $t_j$. The generic path $C_{ij}$ was obtained by averaging the three repeated measurements performed at constant temperature $T_i$ and time instant $t_j$; subsequently, the integral was calculated for each investigated temperature and for each considered time instant to perform the EIS measurements. Finally, for each investigated temperature, the result of the integral $(\alpha_{ij})$ was normalized with respect to the results obtained at the first $(\alpha_{i1})$ and the last $(\alpha_{i10})$ time instant considered, obtaining the normalized

$$\hat{\alpha}_{ij} = \frac{\alpha_{ij} - \alpha_{i10}}{\alpha_{i1} - \alpha_{i10}}, \quad \forall i = 1, 2, 3, 4 \text{ and } j = 1, 2, \dots, 10. \tag{5}$$

Fig. 3 shows the normalized result of the integral $(\hat{\alpha}_{ij})$ for each investigated temperature, as the time instant in which the EIS measurement was performed varies. The obtained results clearly show a common trend for all the investigated temperatures: in fact, a behavior of the electrolyte emerges, analyzed through the area under the Nyquist plot, in a first transitory phase that subsequently tends to reach an equilibrium phase.

The aim of the work is precisely to investigate the time evolution of the electrolyte to reach thermal equilibrium. To this end, the experimental results shown in Fig. 3 have been fitted with the following exponential model

$$\hat{\alpha}_i^* = e^{\frac{-t}{\tau_i}}, \quad \forall i = 1, 2, 3, 4, \tag{6}$$

where $t$ represents the time evolution, $\tau_i$ indicates the time constant of the cell tested at the $i$th temperature, $\hat{\alpha}_i^*$ denotes the fitting result at the $i$th temperature. The fitting operation was performed for each investigated temperature (see $\forall i = 1, 2, 3, 4$). The obtained fitting results are shown in Table 2.

As can be seen from Fig. 3, the fitting operation is excellent and the exponential trend perfectly reflects the nature of the problem. Two important considerations are provided below.

- As previously mentioned, at all the investigated temperatures the reaching of cell's thermal regime presents a non-negligible transitory period (demonstrated by the time constant $\tau$ identified through the exponential fitting). It is very important to highlight this aspect, as it underlines that to perform reliable measurements on this material it is necessary to wait a relatively long time; for example at 700 °C considering the regime phase reached after $5\tau$ it is necessary to wait more than three hours. To the best of the authors' knowledge, no researcher has ever considered this aspect, therefore it represents a strong aspect of novelty that could contribute to significantly increase the knowledge regarding these materials.

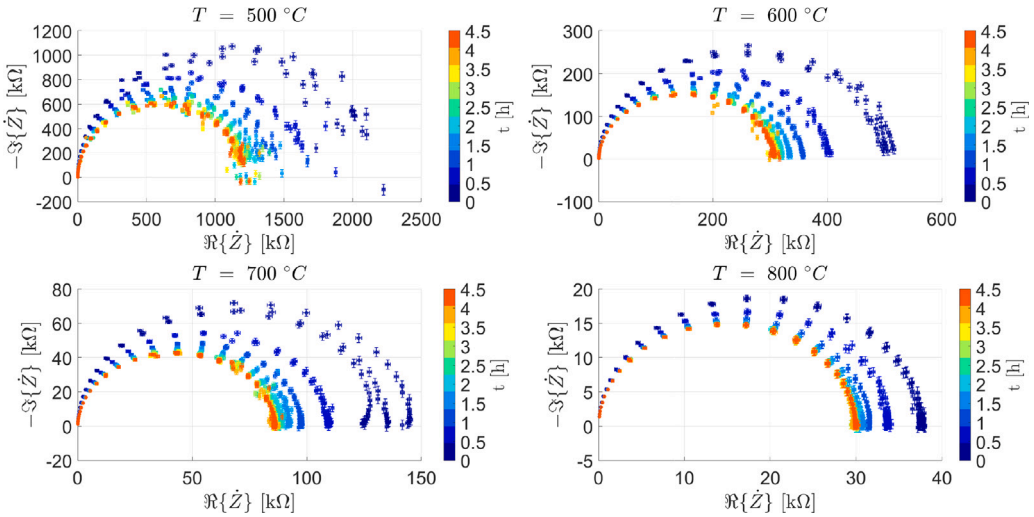


**Fig. 1.** The obtained impedance measurements during the experimental characterization: rectangular representation.

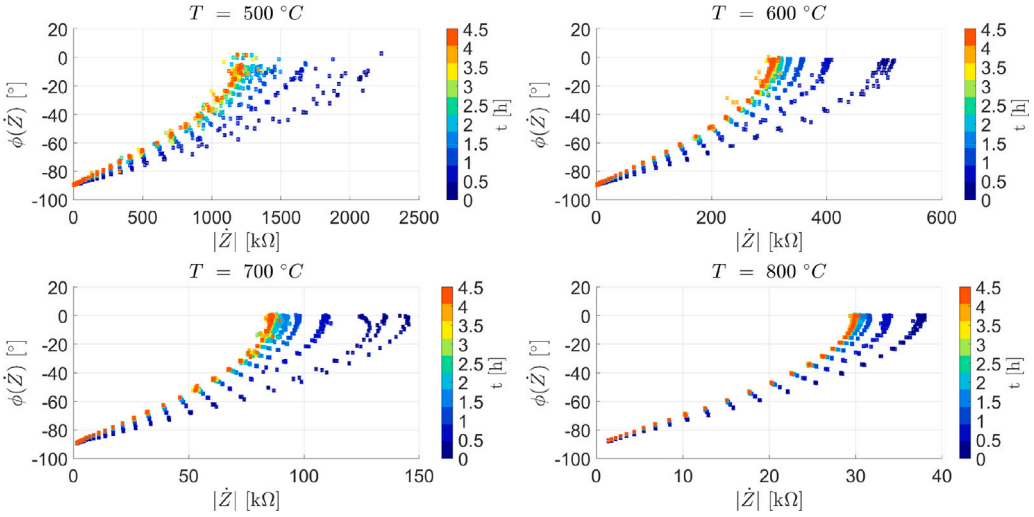


**Fig. 2.** The obtained impedance measurements during the experimental characterization: polar representation.

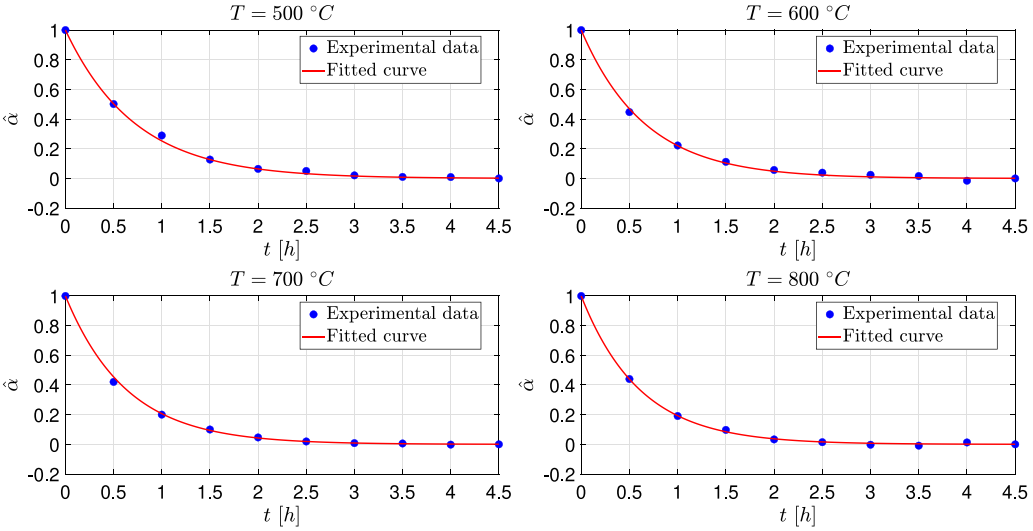


**Fig. 3.** Normalized area under the Nyquist plot for all temperatures and time instants considered.

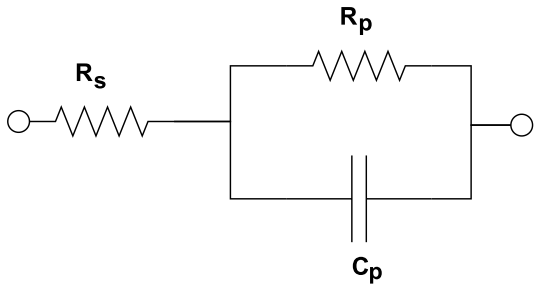


**Fig. 4.** Adopted Randles electrical model.

- Another important consideration is that the thermal dynamics discussed in the previous point is variable with temperature. In fact, the identified time constants are decreasing as the temperature increases, very likely due to the temperature dependence of CZYEN thermal conductivity [37].

In addition, to deepen the phenomenological aspect of the problem, the well-known Randles electrical model shown in Fig. 4 was considered to describe the obtained experimental data. The considered version of the circuit consists of a series resistance $(R_s)$ to model the electrolyte connected to a parallel between a resistance $(R_p)$ and a capacitance $(C_p)$. Such equivalent circuit configuration is typical of ionic-conducting electrolytes at intermediate-high temperature regimes, where grain bulk and grain boundary contributions of the ceramic electrolyte are usually indistinguishable [38].

The parameters of the electrical circuit were identified by strategy based on the resolution of a minimization problem. Specifically, considering the variable $\vartheta = \{R_s, R_p, C_p\}$ that groups the unknowns of the electrical circuit, an objective function $F(\vartheta)$ dependent on $\vartheta$ to be minimized has been defined as follows

$$F(\vartheta) = \sum_{h=1}^{N} \left| \dot{Z}_{model,h}(\vartheta) - \dot{Z}_{meas,h} \right|, \tag{7}$$

where $N$ represents the total number of investigated frequencies, $\dot{Z}_{model,h}(\vartheta)$ represents the theoretical impedance obtained with the Randles model to the $h$th tests frequency and $Z_{meas,h}$ represents the impedance measured to the $h$th test frequency. Finally, the optimal values of the circuit parameters $(\hat{\vartheta})$ were obtained as

$$\hat{\vartheta} = \underset{\vartheta}{\operatorname{argmin}} F(\vartheta), \tag{8}$$

solving the problem in the MATLAB environment using the simplex algorithm [39]. The procedure just described was used to identify the equivalent electrical model for all temperatures and time instants considered. Fig. 5 shows the obtained results in which the goodness of the fitting carried out can be appreciated. Just for the sake of clarity, the last of the three repeated measurements taken for each temperature and time instant considered is analyzed in detail. A more detailed analysis of the goodness of the fitting is performed through Fig. 6 which shows the histograms of the percentage residuals for all the temperatures and time instants considered. It is noteworthy that for all investigated temperatures, a strong residue concentration is observed, significantly lower than 3%, indicating that the model provides very accurate predictions for most cases. However, at very low occurrence frequencies, significant residues around 10% occur, reflecting outliers in the measured data, which the model struggles to predict correctly. These events occur primarily at lower temperatures, such as 500 °C, due to the lower overall responsiveness of the ceramic electrolyte. Finally, Table 3 reports the overall performance, in terms of Root Mean Square Percentage Error ($RMSPE$) of the Randles model identification for all temperatures and time instants considered. $RMSPE$ was calculated as

**Table 3**
Fitting results using the Randles electrical model for all the temperatures and time instants considered.

| T [°C] / t [h] | 500 RMSPE [%] | 600 RMSPE [%] | 700 RMSPE [%] | 800 RMSPE [%] |
|---|---|---|---|---|
| 0.0 | 3.58% | 0.98% | 0.99% | 0.68% |
| 0.5 | 3.11% | 1.76% | 1.08% | 0.64% |
| 1.0 | 2.91% | 0.81% | 0.63% | 0.62% |
| 1.5 | 2.51% | 0.98% | 0.84% | 0.57% |
| 2.0 | 2.60% | 1.03% | 0.73% | 0.58% |
| 2.5 | 2.64% | 1.02% | 1.34% | 0.55% |
| 3.0 | 2.60% | 0.74% | 1.13% | 0.47% |
| 3.5 | 2.83% | 0.98% | 0.81% | 0.60% |
| 4.0 | 3.30% | 2.65% | 1.18% | 0.52% |
| 4.5 | 2.32% | 1.20% | 1.28% | 0.52% |

follows

$$RMSPE = \sqrt{\frac{100}{N} \sum_{h=1}^{N} \left( \frac{\left| \dot{Z}_{model,h} - \dot{Z}_{meas,h} \right|}{\left| \dot{Z}_{meas,h} \right|} \right)^2}. \tag{9}$$

Once the Randles model has been identified, it is possible to analyze the trend of the electrical parameters of the circuit $(R_s, C_p, R_p)$ as the different conditions investigated vary in terms of temperature and time instants used to carry out the impedance measurement. Therefore, Figure S4 within the Supplementary Material shows the evolution of the series resistance $(R_s)$, while Figs. 7 and 8 show the trends of the parallel capacitance $(C_p)$ and parallel resistance $(R_p)$, respectively.

As previously described, the Randles equivalent circuit parameters have been selected for further discussion. In particular, the parameters $C_p$ and $R_p$ were deeply analyzed and, based on typical literature values for $C_p$ [40] (i.e. $10^{-9} \div 10^{-10}$ F), they have been attributed to the grain boundary impedance of the electrolyte. Additionally, $C_p$ exhibits negligible variation with temperature (as observed in Fig. 7), and this behavior can be interpreted by considering its dependance on the microstructure of the fabricated electrolyte (remaining essentially unchanged during the measures due to the "mild" temperature conditions at which it has been subjected), practically preventing any grain growth phenomena influencing grain boundaries extension. The parameter $R_p$ (parallel resistance) represents a parasitic effect of an ideal capacitor limiting the flow of electric current through it. Thus, $R_p$ can be associated with the resistance to carrier transport across the CZYEN grain boundaries [41]. Considering that the series of $R_s$ and $R_p \parallel C_p$ in the Randles circuit models the whole electrolyte response (being it a mixed ionic/electronic conductor) interfaces, and that the electrode/electrolyte interface is "collapsing" in the low-frequency intercept of the Nyquist plot given the non-blocking nature of the Ag electrode towards oxygen [23], it globally models the proneness to let charge transfer across the whole cell occur, consequently modeling the kinetics of all the electrochemical reactions occurring within the system. Increasing values of $R_p$ typically indicate a slowdown in charge transfer processes, often associated with system degradation or the formation of resistive layers. However, we observed a significant decrease of $R_p$ over time, as charge transfer processes at the electrode/electrolyte interfaces speed up upon the observed transitory. Thus, the only physical phenomenon possibly explaining this behavior is the increasing temperature (accelerating chemical reactions, mass transport and, thus, charge transfer) at the electrode/electrolyte interfaces, where metal electrodes almost immediately reach the furnace temperature whilst the ceramic high-entropy electrolyte needs much more time to reach it.

As previously done with the result of the integral of the Nyquist plots, in order to investigate the time evolution of the electrolyte to reach the thermal equilibrium, for each investigated temperature the parallel resistance $(R_{p,ij})$ was normalized with respect to the value obtained at the first $(R_{p,i1})$ and last $(R_{p,i10})$ time instant considered,

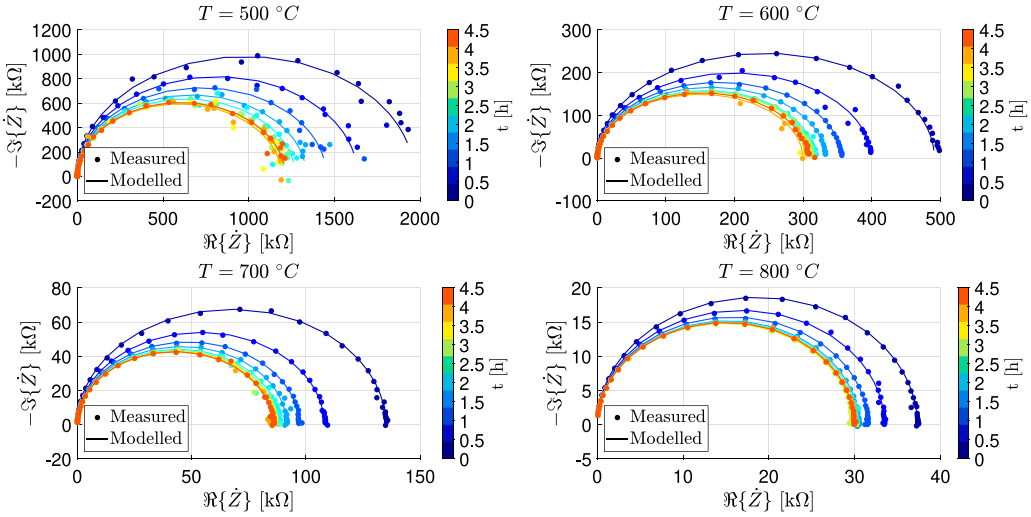


**Fig. 5.** Measured and modeled impedances for all temperatures and time constants considered.

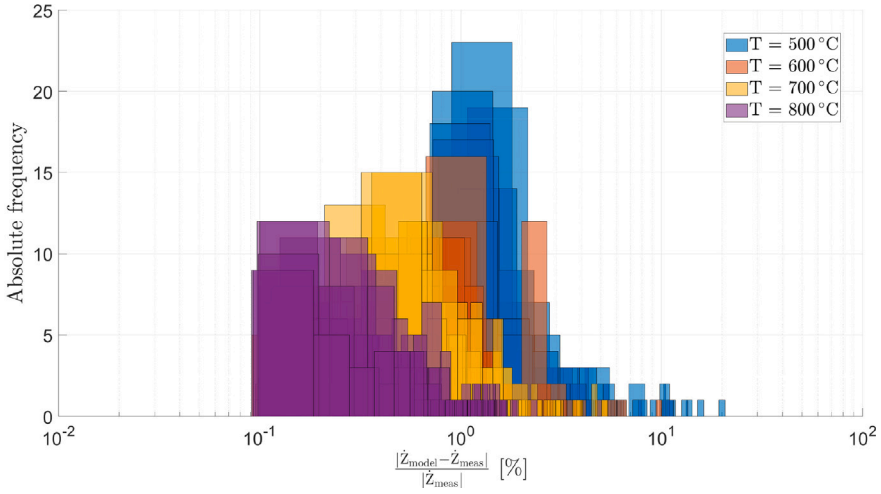


**Fig. 6.** Histograms of the residues obtained for the identification of the Randles electrical model for all the temperatures and time instants considered.

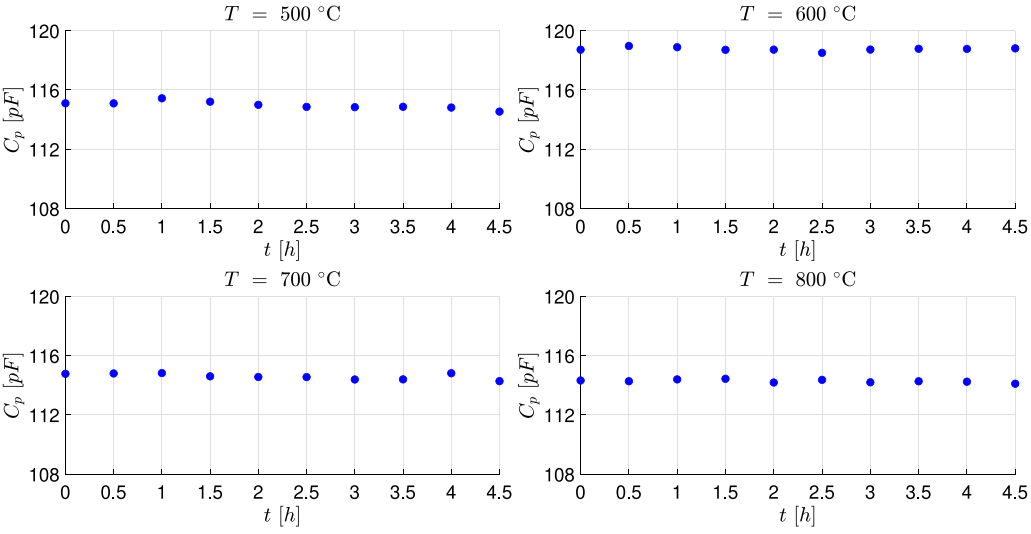


**Fig. 7.** Parallel capacitance for all temperatures and time instants considered.

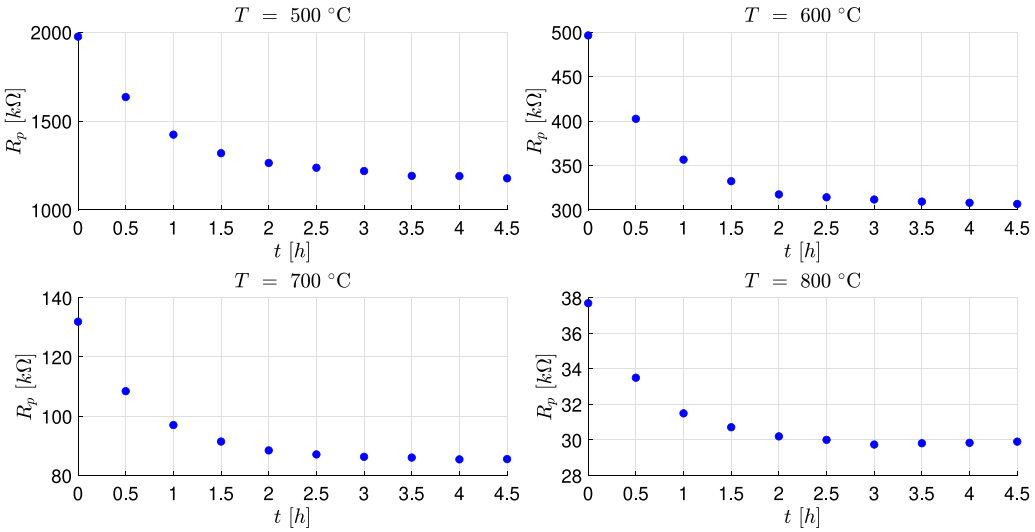


**Fig. 8.** Parallel resistance for all temperatures and time instants considered.

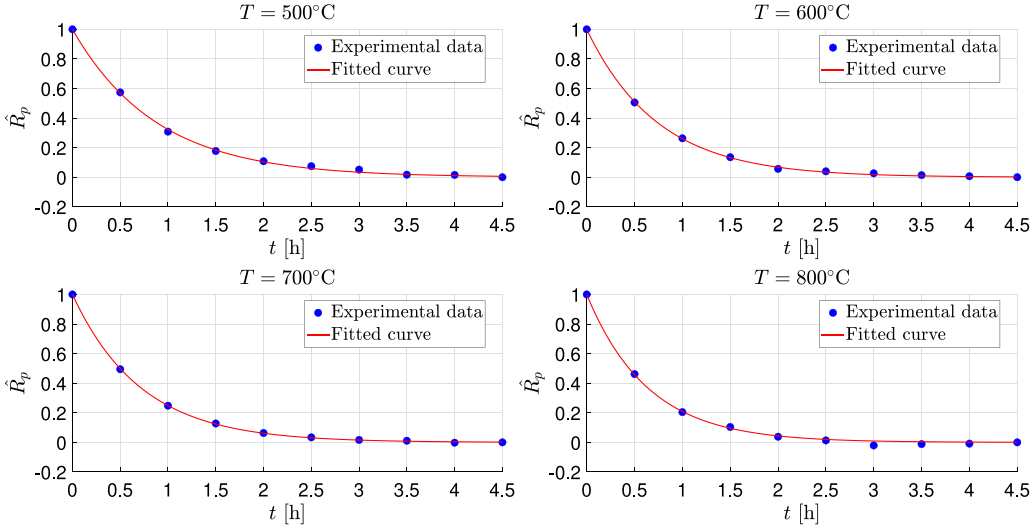


**Fig. 9.** Normalized parallel resistance for all temperatures and time instants considered.

obtaining the normalized $(\hat{R}_{p,ij})$ shown below

$$\hat{R}_{p,ij} = \frac{R_{p,ij} - R_{p,i10}}{R_{p,i1} - R_{p,i10}}, \quad \forall i = 1,2,3,4 \text{ and } j = 1,2,\dots,10. \tag{10}$$

Subsequently, the normalized quantity $\hat{R}_{p,ij}$ has been fitted with the following exponential model

$$\hat{R}^*_{p,i} = e^{\frac{-t}{\tau_i}}, \quad \forall i = 1,2,3,4, \tag{11}$$

where $t$ represents the time evolution, $\tau_i$ indicates the time constant of the cell tested at the $i$th temperature, $\hat{R}^*_{p,i}$ denotes the fitting result at the $i$th temperature. The fitting operation was performed for each investigated temperature (see $\forall i = 1,2,3,4$). The obtained fitting results are shown in Fig. 9 and Table 4.

Also in this case, as can be observed from the obtained results, the fitting operation works very well and the exponential trend perfectly reflects the nature of the problem. The same considerations derived previously can also be obtained in this case. Indeed, for all the investigated temperatures, the measured impedance stabilizes after a few hours, reflecting the considerable importance of considering the evolution of the thermal transient during the characterization processes of these materials. This aspect represents a very important guideline for researchers to use in order to consider the EIS measurement reliable and thus properly characterize the behavior of these materials.

**Table 4**
Fitting output of the normalized parallel resistance using the model shown in (11).

| T [°C] | $\tau$ [h] | RMSE |
|---|---|---|
| 500 | 0.885 | 0.096 |
| 600 | 0.742 | 0.055 |
| 700 | 0.718 | 0.031 |
| 800 | 0.638 | 0.012 |

## 5. Conclusions

The present study has revealed the presence of a significant thermal transient during Electrochemical Impedance Spectroscopy (EIS) measurements on rare-earth-based high-entropy oxide solid electrolytes, tested in a symmetric Ag|$CZYEN$|Ag configuration. Such a transient behavior, consistently observed in the spectral response over time, is intrinsically linked to the thermal properties of the studied material, particularly its low thermal diffusivity, and to the resulting delay in reaching thermal equilibrium with respect to the furnace

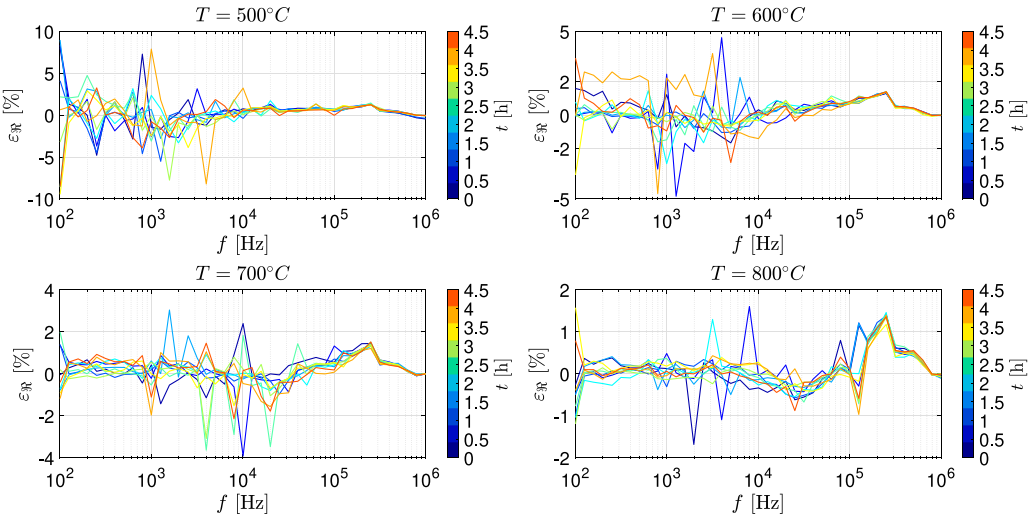


**Fig. A.10.** Obtained performance on the real part of the measured impedances by validation using the Lin-KK method.

temperature. A dedicated analytical model, based on an exponential evolution of impedance parameters, was developed to quantitatively describe this phenomenon and to extract characteristic time constants associated with thermal equilibration. The results clearly indicate that, within the investigated temperature range, EIS measurements require a substantially prolonged waiting period before the electrolyte's temperature aligns with that of the furnace, ensuring reliable and physically meaningful data. These findings emphasize the necessity of re-evaluating conventional experimental protocols for electrochemical characterization of low-diffusivity ceramic electrolytes, particularly within emerging classes of high-entropy oxides.

## CRediT authorship contribution statement

**Filippo Milano:** Writing – review & editing, Writing – original draft, Software, Methodology, Investigation, Data curation, Conceptualization. **Antonio Vendittelli:** Writing – original draft, Validation, Formal analysis, Data curation. **Luca Spiridigliozzi:** Writing – review & editing, Writing – original draft, Validation, Methodology, Investigation, Formal analysis, Conceptualization. **Viviana Monfreda:** Writing – review & editing, Validation, Investigation, Formal analysis. **Gianfranco Dell'Agli:** Writing – review & editing, Validation, Supervision, Methodology, Formal analysis, Conceptualization. **Luigi Ferrigno:** Writing – review & editing, Validation, Supervision, Project administration, Formal analysis, Conceptualization.

## Declaration of competing interest

The authors declare that they have no known competing financial interests or personal relationships that could have appeared to influence the work reported in this paper.

## Acknowledgments

This study was carried out within the MOST – Sustainable Mobility Center and received funding from the European Union NextGenerationEU (PIANO NAZIONALE DI RIPRESA E RESILIENZA (PNRR) – MISSIONE 4 COMPONENTE 2, INVESTIMENTO 1.4 – D.D. 1033 17/06/2022, CN00000023). This manuscript reflects only the authors' views and opinions; neither the European Union nor the European Commission can be considered responsible for them.

This research was also partially funded by the Italian "Ministero dell'Università e della Ricerca" within the "Piano Nazionale di Ripresa e Resilienza (PNRR)" co-financed by the European Union—Next Generation EU—Mission 4 Component 2 Investimento 1.1—2022KWSRSA—CUP H53D23004600006.

## Appendix. Validation of measured impedance data

The validity of the impedances measured through Electrochemical Impedance Spectroscopy is subject to the constraints of a linear time invariant dynamical system, i.e. the conditions of linearity, stationarity and causality that must be respected by the electrochemical system under examination (Ag|$CZYEN$|Ag) [42]. To verify compliance with these requirements, the Kramer-Kronig relations were used via the Lin-KK method [43]. The application of this methodology presupposes a mathematical model of the electrochemical system; for this purpose, the Randles electrical model shown in Fig. 4 was used. The reliability of the measured data is verified by evaluating the difference between the measured impedances and the impedances predicted by the adopted model (Randles model). To this end, the analysis was conducted using the relative errors on the real $\varepsilon_{\Re}(f)$ and imaginary $\varepsilon_{\Im}(f)$ parts, calculated as follows:

$$\varepsilon_{\Re}(f) = \frac{\Re\{\dot{Z}_{meas}(f) - \dot{Z}_{model}(f)\}}{|\dot{Z}_{meas}(f)|} \cdot 100, \tag{A.1}$$

$$\varepsilon_{\Im}(f) = \frac{\Im\{\dot{Z}_{meas}(f) - \dot{Z}_{model}(f)\}}{|\dot{Z}_{meas}(f)|} \cdot 100. \tag{A.2}$$

Figs. A.10 and A.11 show the obtained error trends as the frequency varies and for all the time and temperature conditions investigated. For both the real and imaginary components, the obtained errors improve as the temperature increases (an aspect also highlighted previously, due to the lower overall reactivity of the ceramic electrolyte) and remain within an acceptable range (maximum ± 5 % from 600 °C to 800 °C). This result attests to the reliability of the conducted analysis. At 500 °C, some spot frequency measurements are noted that have a slightly higher deviation, especially at low frequencies, due to the reasons already discussed.

## Appendix B. Supplementary data

Supplementary material related to this article can be found online at https://doi.org/10.1016/j.measurement.2026.120757.

## Data availability

Data will be made available on request.

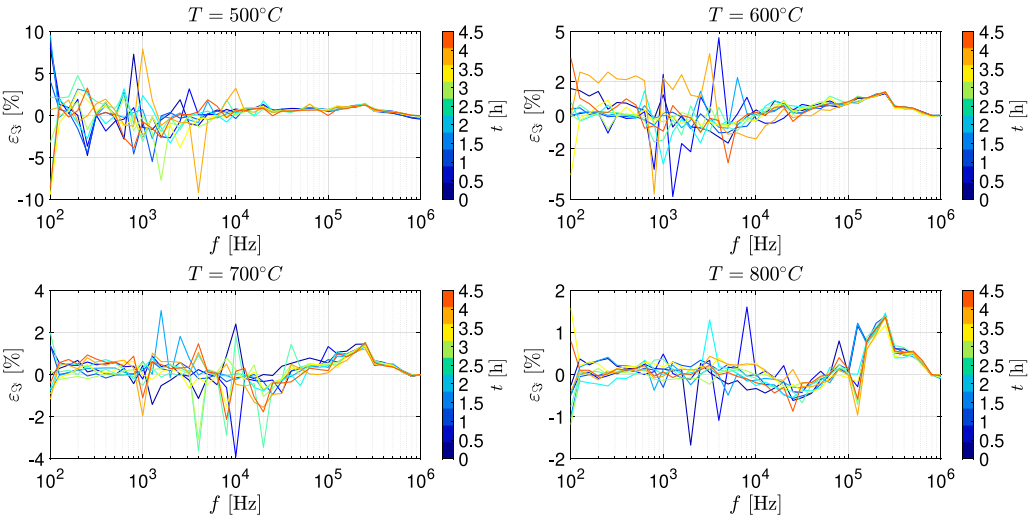


**Fig. A.11.** Obtained performance on the imaginary part of the measured impedances by validation using the Lin-KK method.

## References


[1] J.W. Fergus, Oxide anode materials for solid oxide fuel cells, Solid State Ion. 177 (17–18) (2006) 1529–1541.

[2] E.D. Wachsman, K.T. Lee, Lowering the temperature of solid oxide fuel cells, Science 334 (6058) (2011) 935–939.

[3] A. Lasia, Electrochemical impedance spectroscopy and its applications, in: Modern Aspects of Electrochemistry, Springer, 2002, pp. 143–248.

[4] C. Bourelly, M. Vitelli, F. Milano, M. Molinara, F. Fontanella, L. Ferrigno, Ga-based features selection for electro-chemical impedance spectroscopy on lithium iron phosphate batteries, in: 2023 IEEE International Conference on Electrical Systems for Aircraft, Railway, Ship Propulsion and Road Vehicles & International Transportation Electrification Conference, ESARS-ITEC, IEEE, 2023, pp. 1–6.

[5] H. Mustafa, C. Bourelly, M. Vitelli, F. Milano, M. Molinara, L. Ferrigno, SoC estimation on Li-ion batteries: A new EIS-based dataset for data-driven applications, Data Brief 57 (2024) 110947.

[6] M.R. Baidillah, R. Riyanto, P. Busono, S. Karim, R. Febryarto, A. Astasari, D. Sangaji, W.P. Taruno, Electrical impedance spectroscopy for skin layer assessment: A scoping review of electrode design, measurement methods, and post-processing techniques, Measurement 226 (2024) 114111, http://dx.doi.org/10.1016/j.measurement.2023.114111, URL https://www.sciencedirect.com/science/article/pii/S0263224123016755.

[7] A. Kruk, D. Madej, A new approach to time-resolved electrochemical impedance spectroscopy using the impedance camera to track fast hydration processes in cement-based materials, Measurement 205 (2022) 112199, http://dx.doi.org/10.1016/j.measurement.2022.112199, URL https://www.sciencedirect.com/science/article/pii/S0263224122013951.

[8] J.R. Macdonald, Impedance spectroscopy: Models, data fitting, and analysis, Solid State Ion. 176 (25–28) (2005) 1961–1969.

[9] E. Skou, T. Jacobsen, A model for the frequency dispersion of the impedance of compressed powders of ionic conductors, Appl. Phys. A 49 (1989) 117–121.

[10] J. Jamnik, J. Maier, Nanocrystallinity effects in lithium battery materials aspects of nano-ionics. Part IV, Phys. Chem. Chem. Phys. 5 (23) (2003) 5215–5220.

[11] W. Wang, C. Su, Y. Wu, R. Ran, Z. Shao, Progress in solid oxide fuel cells with nickel-based anodes operating on methane and related fuels, Chem. Rev. 113 (10) (2013) 8104–8151.

[12] D. Yang, G. Chen, H. Liu, L. Zhang, Y. He, X. Zhang, K. Yu, S. Geng, Y. Li, Electrochemical performance of a Ni0. 8Co0. 15Al0. 05LiO2 cathode for a low temperature solid oxide fuel cell, Int. J. Hydrog. Energy 46 (17) (2021) 10438–10447.

[13] B.A. Boukamp, A nonlinear least squares fit procedure for analysis of immittance data of electrochemical systems, Solid State Ion. 20 (1) (1986) 31–44.

[14] B.C. Steele, Appraisal of Ce1- yGdyO2- y/2 electrolytes for IT-SOFC operation at 500°C, Solid State Ion. 129 (1–4) (2000) 95–110.

[15] M. Schönleber, D. Klotz, E. Ivers-Tiffée, A method for improving the robustness of linear Kramers-Kronig validity tests, Electrochim. Acta 131 (2014) 20–27.

[16] M. Brahlek, M. Gazda, V. Keppens, A.R. Mazza, S.J. McCormack, A. Mielewczyk-Gryń, B. Musico, K. Page, C.M. Rost, S.B. Sinnott, et al., What is in a name: Defining "high entropy" oxides, APL Mater. 10 (11) (2022).

[17] S.J. McCormack, A. Navrotsky, Thermodynamics of high entropy oxides, Acta Materialia 202 (2021) 1–21, http://dx.doi.org/10.1016/j.actamat.2020.10.043, Publisher Copyright: © 2020 Acta Materialia Inc..

[18] C.M. Rost, E. Sachet, T. Borman, A. Moballegh, E.C. Dickey, D. Hou, J.L. Jones, S. Curtarolo, J.-P. Maria, Entropy-stabilized oxides, Nat. Commun. 6 (1) (2015) 8485.

[19] X. Ping, B. Meng, X. Yu, Z. Ma, X. Pan, W. Lin, Structural, mechanical and thermal properties of cubic bixbyite-structured high-entropy oxides, Chem. Eng. J. 464 (2023) 142649.

[20] M.R. Levy, C.R. Stanek, A. Chroneos, R.W. Grimes, Defect chemistry of doped bixbyite oxides, Solid State Sci. 9 (7) (2007) 588–593.

[21] A. Chroneos, M. Levy, C.R. Stanek, K. McClellan, R. Grimes, Intrinsic defect processes in bixbyite sesquioxides, Phys. Status Solidi C 4 (3) (2007) 1213–1216.

[22] J.A. Lussier, G. Devitt, K.M. Szkop, M. Bieringer, Oxygen trapping and cation site-splitting in Y (2- x) $PrxO_3+\ \delta$ ($0.0 \leq x < 2.0$ and $\delta \leq 1.0$), J. Solid State Chem. 242 (2016) 126–132.

[23] X. Kuang, M.A. Green, H. Niu, P. Zajdel, C. Dickinson, J.B. Claridge, L. Jantsky, M.J. Rosseinsky, Interstitial oxide ion conductivity in the layered tetrahedral network melilite structure, Nat. Mater. 7 (6) (2008) 498–504.

[24] L. Xu, H. Wang, L. Su, D. Lu, K. Peng, H. Gao, A new class of high-entropy fluorite oxides with tunable expansion coefficients, low thermal conductivity and exceptional sintering resistance, J. Eur. Ceram. Soc. 41 (13) (2021) 6670–6676.

[25] D. Liu, B. Shi, L. Geng, Y. Wang, B. Xu, Y. Chen, High-entropy rare-earth zirconate ceramics with low thermal conductivity for advanced thermal-barrier coatings, J. Adv. Ceram. 11 (6) (2022) 961–973.

[26] L. Spiridigliozzi, V. Monfreda, A. Marocco, F. Milano, A. Vendittelli, G. Dell'Agli, Effect of synthesis and processing conditions on the sintering behavior and total conductivity of high-entropy fluorite/bixbyite oxides (RE-HEOs), Materials 18 (11) (2025) 2663.

[27] M.V. Kante, A.R.L. Nilayam, K. Kreka, H. Hahn, S.S. Bhattacharya, L. Velasco, A. Tarancón, C. Kübel, S. Schweidler, M. Botros, Influence of Zr-doping on the structure and transport properties of rare earth high-entropy oxides, J. Phys.: Energy 6 (3) (2024) 035001.

[28] Y. Sun, H. Xiang, F.-Z. Dai, X. Wang, Y. Xing, X. Zhao, Y. Zhou, Preparation and properties of CMAS resistant bixbyite structured high-entropy oxides RE2O3 (RE=Sm, Eu, Er, Lu, Y, and Yb): Promising environmental barrier coating materials for Al2O3f/Al2O3 composites, J. Adv. Ceram. 10 (3) (2021) 596–613.

[29] A. Mancuso, K. Monzillo, O. Sacco, L. Spiridigliozzi, V. Monfreda, A. Muscatello, G. Dell'Agli, S. Esposito, V. Vaiano, Engineered synthesis of a novel bixbyite-structured high-entropy oxide (Ce0. 2Zr0. 2Yb0. 2Er0. 2Gd0. 2) 2O3. 4 as a stable and high-performing visible-light-active photocatalyst for multifunctional pollutant degradation, J. Alloys Compd. 1026 (2025) 180435.

[30] L. Spiridigliozzi, C. Ferone, R. Cioffi, G. Dell'Agli, A simple and effective predictor to design novel fluorite-structured high entropy oxides (HEOs), Acta Mater. 202 (2021) 181–189.

[31] G. Accardo, G. Dell'Agli, L. Spiridigliozzi, S.P. Yoon, D. Frattini, On the oxygen vacancies optimization through Pr co-doping of ceria-based electrolytes for electrolyte-supported solid oxide fuel cells, Int. J. Hydrog. Energy 45 (38) (2020) 19707–19719.

[32] L. Spiridigliozzi, V. Monfreda, A. Marocco, G. Dell'Agli, On the effect of kinetics on the formation of fluorite/bixbyite-structured entropy-stabilized oxides, Ceramics International (2025).

[33] C. Suryanarayana, M.G. Norton, X-rays and diffraction, in: X-Ray Diffraction: A Practical Approach, Springer, 1998, pp. 3–19.

[34] M. Shamsuddin, Thermodynamic Measurement Techniques, Springer, 2024.

[35] Gamry reference 3000 instrument reference site, 2025, https://www.gamry.com/potentiostats/reference/reference-3000/. (Accessed 18 June 2015).

[36] J. Ordonez-Miranda, M. Hermens, I. Nikitin, V.G. Kouznetsova, O. van der Sluis, M.A. Ras, J.S. Reparaz, M. Wagner, M. Sledzinska, J. Gomis-Bresco, et al., Measurement and modeling of the effective thermal conductivity of sintered silver pastes, Int. J. Therm. Sci. 108 (2016) 185–194.

[37] F. Li, L. Zhou, J.-X. Liu, Y. Liang, G.-J. Zhang, High-entropy pyrochlores with low thermal conductivity for thermal barrier coating materials, J. Adv. Ceram. 8 (2019) 576–582.

[38] G. Accardo, G.D. Agli, D. Frattini, L. Spiridigliozzi, S.W. Nam, S.P. Yoon, Electrical behaviour and microstructural characterization of magnesia co-doped ScSZ nanopowders synthesized by urea co-precipitation, Chem. Eng. Trans. 57 (2017) 1345–1350.

[39] J.C. Lagarias, J.A. Reeds, M.H. Wright, P.E. Wright, Convergence properties of the Nelder–Mead simplex method in low dimensions, SIAM J. Optim. 9 (1) (1998) 112–147.

[40] J.T. Irvine, D.C. Sinclair, A.R. West, Electroceramics: characterization by impedance spectroscopy, Adv. Mater. 2 (3) (1990) 132–138.

[41] M. Gerstl, E. Navickas, G. Friedbacher, F. Kubel, M. Ahrens, J. Fleig, The separation of grain and grain boundary impedance in thin yttria stabilized zirconia (YSZ) layers, Solid State Ion. 185 (1) (2011) 32–41.

[42] N. Hallemans, D. Howey, A. Battistel, N.F. Saniee, F. Scarpioni, B. Wouters, F. La Mantia, A. Hubin, W.D. Widanage, J. Lataire, Electrochemical impedance spectroscopy beyond linearity and stationarity—A critical review, Electrochim. Acta 466 (2023) 142939.

[43] M. Schönleber, D. Klotz, E. Ivers-Tiffée, A method for improving the robustness of linear Kramers-Kronig validity tests, Electrochim. Acta 131 (2014) 20–27, http://dx.doi.org/10.1016/j.electacta.2014.01.034, Electrochemical Impedance Spectroscopy. URL https://www.sciencedirect.com/science/article/pii/S0013468614001005.